Catalysis Science & Technology

ROYAL SOCIETY OF CHEMISTRY

PAPER

View Article Online
View Journal | View Issue

Cite this: *Catal. Sci. Technol.*, 2025, 15, 4988

Solid micellar catalysts: exploring the stability of $Ru^{(III)}$ single-sites in amorphous silica†

Sara Santos, [a] Vitaly V. Ordomsky, [b] Frederik Tielens [c] and Mark Saeys *[a]

Amorphous silica plays an important role as a catalyst support due to its structural and chemical properties, though its complexity poses challenges identifying and characterizing active sites. Computational models capturing the heterogeneity of amorphous silica-supported materials are crucial in understanding these systems and their catalytic behavior. $Ru^{(III)}$@MCM-41, the first example of a solid micellar catalyst, consists of $Ru^{(III)}$ sites and silanoxo basic sites incorporated into the walls of amorphous MCM-41 and stabilized by quaternary ammonium surfactant molecules (CTA^+) in the pores. To link structure and activity, computational models were developed to elucidate the nature and activity of these $Ru^{(III)}$ single-sites. The amorphous silica framework offers a wide heterogeneity of sites where ruthenium can be located. To understand how site distribution affects the activity and stability of $Ru^{(III)}$ sites, a periodic model of an amorphous hydroxylated silica surface was used. The model includes 27 potential Si-to-$Ru^{(III)}$ exchange and multiple $Ru^{(III)}$ grafting sites, from bulk-like $Si(O)_4$ to single and geminal silanol groups ($Si(O)_3(OH)$ and $Si(O)_2(OH)_2$, respectively). The coordination environment, ring strain, and the hydrogen bonding interactions influence the stability and activity of the $Ru^{(III)}$ single-sites. Incorporating $Ru^{(III)}$ in amorphous silica is highly favorable, with Si-to-$Ru^{(III)}$ exchange energies up to −248 kJ mol^{-1} in the presence of the CTA^+ surfactant. Replacing the surfactant counterion with H^+ results in a less favorable incorporation of $Ru^{(III)}$, with exchange energies up to −118 kJ mol^{-1}, highlighting the surfactant's stabilizing role. Grafting of $Ru^{(III)}$ onto silanoxo groups is also favorable in the presence of surfactant. However, space restrictions and the limited availability of neighboring silanol groups at an optimal distance made the formation of $Ru^{(III)}(O)_4$ challenging, instead favoring less stable $Ru^{(III)}(O)_2(OH)_2$ species. Our calculations suggest that $Ru^{(III)}$ is predominantly present as $Ru^{(III)}(O)_4(H_2O)_2$ or $Ru^{(III)}(O)_3(OH)(H_2O)_2$ at sites within large Si-membered rings near hydroxylated regions. Various $Ru^{(III)}$-hydride species were calculated, with formation energies ranging from +21 to −113 kJ mol^{-1}. Interestingly, some highly stable $Ru^{(III)}$ sites also show favorable hydride formation, making them both synthesizable and active.

Received 11th April 2025,
Accepted 13th July 2025

DOI: 10.1039/d5cy00449g

rsc.li/catalysis

1. Introduction

Amorphous silica is a versatile material, widely used as a support for solid catalysts.[1,2] Its structural disorder, thermal stability and lack of strong metal–support interactions offer unique advantages for catalytic applications. However, its complex and non-crystalline structure, which is highly sensitive to synthesis conditions, presents challenges for characterization and reliable molecular modelling.[1]

Efforts to model amorphous silica have focused on cluster and periodic slab models. Cluster models, carved from optimized bulk materials, are useful to investigate the local nature of active sites, their immediate environment and in unraveling complete catalytic cycles.[1,3–7] While clusters represent the local structure and certain aspects of amorphous silica, there are limitations in addressing geometric factors (*e.g.*, ring sizes) and long-range effects, such as interactions between neighboring silanol groups and hydrogen bonding. Larger periodic models are better suited to account for the heterogeneity and distribution of sites by incorporating long-range electronic and geometric effects, and can account for the non-local changes in the structure and in the H-bonded networks (hydroxyl nests) due to the incorporation of active sites.[8] Crystalline materials, such as β-cristobalite, have been used to model amorphous silica, but this approach fails to sufficiently capture the material's non-uniform structural diversity.[3]

[a] *Laboratory for Chemical Technology (LCT), Department of Materials, Textiles and Chemical Engineering, Ghent University, Technologiepark 125, 9052 Gent, Belgium. E-mail: mark.saeys@ugent.be*
[b] *UCCS – Unité de Catalyse et Chimie du Solide, Université de Lille, CNRS, Centrale Lille, ENSCL, Université d'Artois, UMR, 8181 Lille, France*
[c] *General Chemistry (ALGC), Materials Modelling Group, Vrije Universiteit Brussel, Pleinlaan 2, Brussel, Belgium*

† Electronic supplementary information (ESI) available. See DOI: https://doi.org/10.1039/d5cy00449g

The cleaved surface of bulk amorphous silica shows uncoordinated atoms, including three coordinated silicon atoms, terminal non-bridging oxygens, and strained Si–O–Si bridges.[9,10] When exposed to water, these structural defects result in the formation of surface hydroxyl groups – silanol groups – which define the reactivity and hydrophobicity of the hydroxylated silica surface. They can be classified as single or geminal, depending on whether one or two OH groups are bonded to a single silicon atom. Additionally, their classification also considers their involvement in hydrogen bonding. Silanols can exist either in isolated forms or as part of hydroxyl nests, where they participate in hydrogen bonding with neighboring silanols, siloxane bridges, or solvent molecules.[9–11]

Modelling amorphous silica, particularly as a support for transition metal oxide catalysts, has advanced significantly since the development of realistic periodic models.[9,12–14] These models incorporate experimental data on Si–O bond lengths, Si–O–Si bond angles, ring size distribution, and the density and distribution of silanol groups, that align with NMR parameters and OH vibrational frequencies from several silicalite materials.[9] Other periodic models vary the silanol density by developing partially and fully dehydroxylated amorphous silica surface models that represent these materials at higher temperatures.[13,14] An accurate description of the silica surface, particularly the type, distribution and number of silanols, is essential because these groups serve as anchoring points for grafting metal oxides. Periodic slab models have been used to study mostly the grafting of metal oxides and clusters in partially dehydroxylated and hydroxylated amorphous silica surfaces and for mechanistic studies.[15–23] These models have provided valuable insights into the structure and reactivity of supported transition metal oxides. A recent study expanded on this by investigating the adsorption behavior of various late-transition metals on silica rings of varying sizes and degrees of hydroxylation.[24]

SOlid MICellar (SOMIC) catalysts are a complex class of heterogeneous catalytic materials, consisting of isolated active sites incorporated in an amorphous silica framework and stabilized by surfactant molecules that remain within the pores. The first SOMIC catalyst to be synthesized and characterized – $Ru^{(III)}$@MCM-41 – consists of single $Ru^{(III)}$ atoms and silanoxo basic sites ($Si–O^-$) incorporated into the walls of MCM-41, and stabilized by quaternary ammonium surfactant molecules (cetyltrimethylammonium cation, CTA^+) in the pores. This catalyst has demonstrated high activity for the selective hydrogenation of carbonyl bonds and CO_2 to alcohols and formate, respectively, performing comparably to state-of-the-art homogeneous Ru catalysts while offering superior stability and recyclability.[25–27] A particular feature of this material is the presence of the surfactant within the pores. Experimental studies have shown that removing or replacing the surfactant, results in a significant reduction in catalyst stability and activity.[25]

The synthesis of $Ru^{(III)}$@MCM-41 is based on the MCM-41 preparation method and is simpler than most single-atom catalyst synthesis strategies. The procedure starts by mixing the surfactant molecules (cetyltrimethylammonium bromide, CTAB) in a ethanol/water solution to form micelles. Above the critical micellar concentration, the micellar structure aggregates into rod-shaped micelles, which serve as the template for the mesopores (Fig. 1). These micelles are then combined with the metal precursor $Ru^{(III)}Cl_3$ in an aqueous solution. The silica precursor tetraethyl orthosilicate (TEOS) is then added, undergoing hydrolysis and condensation. This allows the silica to condense around the micellar structures, incorporating $Ru^{(III)}$, and form a framework under basic conditions. The final result is an ordered, hexagonal mesoporous structure, with 3.1 wt% $Ru^{(III)}$ incorporated into the amorphous silica walls ($Si/Ru^{(III)}$ ratio of 15) and the surfactant molecules retained within the pores ($CTA^+/Ru^{(III)}$ ratio of 4, Fig. 1).

Previous work on $Ru^{(III)}$@MCM-41 focused on modelling the active site using cluster models based on silsesquioxane cages.[25,26] These studies revealed that $Ru^{(III)}$ single-sites behave like homogeneous $Ru^{(III)}$ within a heterogeneous silica framework. Moreover, they provided insight into the reaction mechanism, particularly highlighting the formation of $Ru^{(III)}$-hydride species as a key step in hydrogenation reactions.[25,26] While this approach enhanced our understanding of the catalyst activity, it is limited in its ability to account for the diversity of $Ru^{(III)}$ sites and long-range interactions, such as hydrogen bonding, within the amorphous silica structure.

A comprehensive study using periodic slab models is required to capture the complexity of the material and gain a deeper insight into the stabilizing effect of the surfactant. To the best of our knowledge, no existing amorphous silica surface models include surfactant molecules, which are critical for explaining the stability and activity of $Ru^{(III)}$ sites. To address this further, we exchanged the CTA^+ counterion with a proton in the model to simulate the absence of surfactant.

Our modelling strategy focuses on the Si-to-$Ru^{(III)}$ exchange in a state-of-the-art hydroxylated amorphous silica surface. Si-to-$Ru^{(III)}$ exchange involves replacing each Si site with $Ru^{(III)}$ and a counterion to balance the charge. This systematic approach allows to calculate the relative stability of all 27 available $Ru^{(III)}$ sites within the amorphous silica walls using a well-defined silica reference. We also considered the possibility of grafted $Ru^{(III)}$ sites, where $[Ru^{(III)}(OH)_4(H_2O)_2]^-$ condenses with silanol groups available on the amorphous silica slab. Our theoretical investigation helps identify favorable $Ru^{(III)}$ single-sites and their activity within the solid micellar $Ru^{(III)}$@MCM-41 catalyst.

2. Computational methods

Periodic density functional theory (DFT) calculations were performed using the Vienna *ab initio* simulation package (VASP, version 6.4.2).[28] Geometry optimizations were performed using the Perdew–Burke–Ernzerhof (PBE)

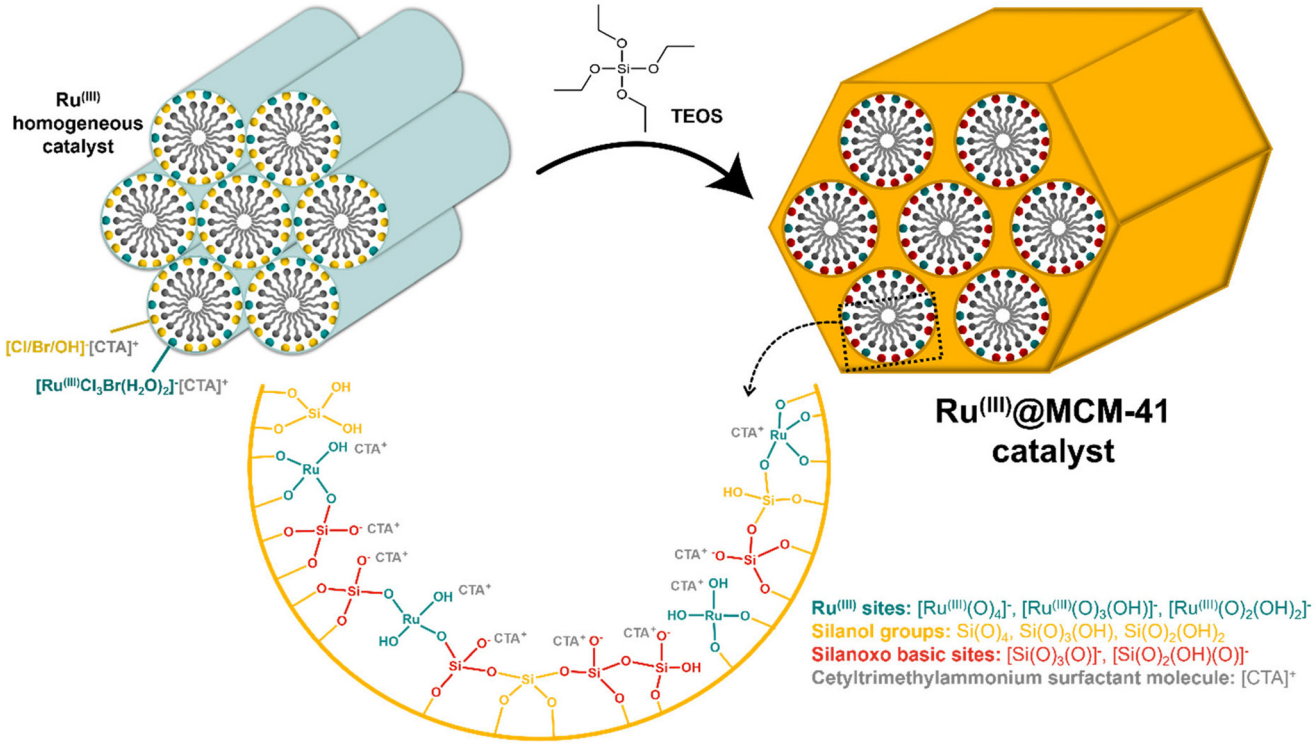

Fig. 1 Scheme of the synthesis of Ru$^{(III)}$@MCM-41 and the type of sites found in the amorphous Ru$^{(III)}$@MCM-41 catalyst.

functional,[29] including Grimme DFT-D3 empirical dispersion with the Becke–Johnson (BJ) damping function[30] to account for non-covalent interactions. Electron–ion interactions were described by the projector augmented-wave (PAW) method[31] with a cutoff energy of 400 eV. A single gamma-centered *k*-point grid was applied in all calculations due to the large size of the supercell, while the partial occupancies for each wave function are set using the Gaussian smearing method. The positions of all atoms in the unit cell were fully relaxed during geometry optimizations, and the electronic convergency criterion was set at 10^{-5} eV.

Benchmark calculations were conducted on molecular complexes representing the Si–O–Si and Si–O–Ru bonds using the ORCA program package (version 5.0.4).[32] Geometry optimizations were also carried out with the Perdew–Burke–Ernzerhof (PBE) functional, incorporating Grimme's D3 dispersion corrections and Becke–Johnson (BJ) damping functions, with Ahlrichs' Def2-TZVP basis set.[33] Single-point electronic energy calculations were performed using the high-level domain-based local pair natural orbital coupled-cluster method DLPNO-CCSD(T)[34] for the optimized structures. For these calculations, the Def2-TZVP basis set and the corresponding Def2-TZVP/C auxiliary basis set were applied.

The stability of water was obtained from a cluster of four molecules of H_2O, as previous work showed that small cluster structures containing 3 to 5 molecules of H_2O are stable and sufficient to model the desorbed water not interacting with the catalyst surface.[26]

The amorphous hydroxylated silica surface model used in this study was developed by Tielens and coworkers (Fig. 2a).[9] The unit cell dimensions are a = 12.77 Å, b = 17.64 Å and c = 25.17 Å (including 15 Å of vacuum). The unit cell corresponds to $Si_{27}O_{41}(OH)_{26}$, with a total of 120 atoms and a silanol density of 5.8 OH nm^{-2}.

The silica model structure is composed of interconnected SiO_2 rings of various sizes, ranging from 4- to 10-membered rings (Fig. 2b–d). The model includes 27 Si atoms in different coordination environments: 6 bulk-like $Si(O)_4$, 16 single silanol $Si(O)_3(OH)$ and 5 geminal silanol $Si(O)_2(OH)_2$ groups (Fig. 3). Silanol groups can be classified as either isolated (non-H-bonded) or involved in hydrogen bonding (H-bonded), as illustrated in Fig. 3.

Additional studies on the suitability of the model size and level of theory are presented in Tables S1–S3 and part III of the ESI.† These include a larger supercell, composed of $Si_{108}O_{164}(OH)_{104}$ (Fig. S1†), which was constructed by expanding the 27 Si atom periodic model into a (2 × 2 × 1) unit cell, as well as cluster models and ring structures carved from the amorphous silica structure (Fig. S2†)

The most active Ru$^{(III)}$@MCM-41 catalyst contains 3.1 wt% of ruthenium, corresponding to a Si/Ru$^{(III)}$ ratio of 15, or about two Ru$^{(III)}$ active sites per unit cell in our model. The CTA$^+$/Ru$^{(III)}$ ratio in the synthesized material is 4, indicating that, in addition to the two Ru$^{(III)}$ active sites, there could be six silanoxo base sites (Si–O$^-$) each interacting with a surfactant molecule per unit cell.[25] These silanoxo-surfactant

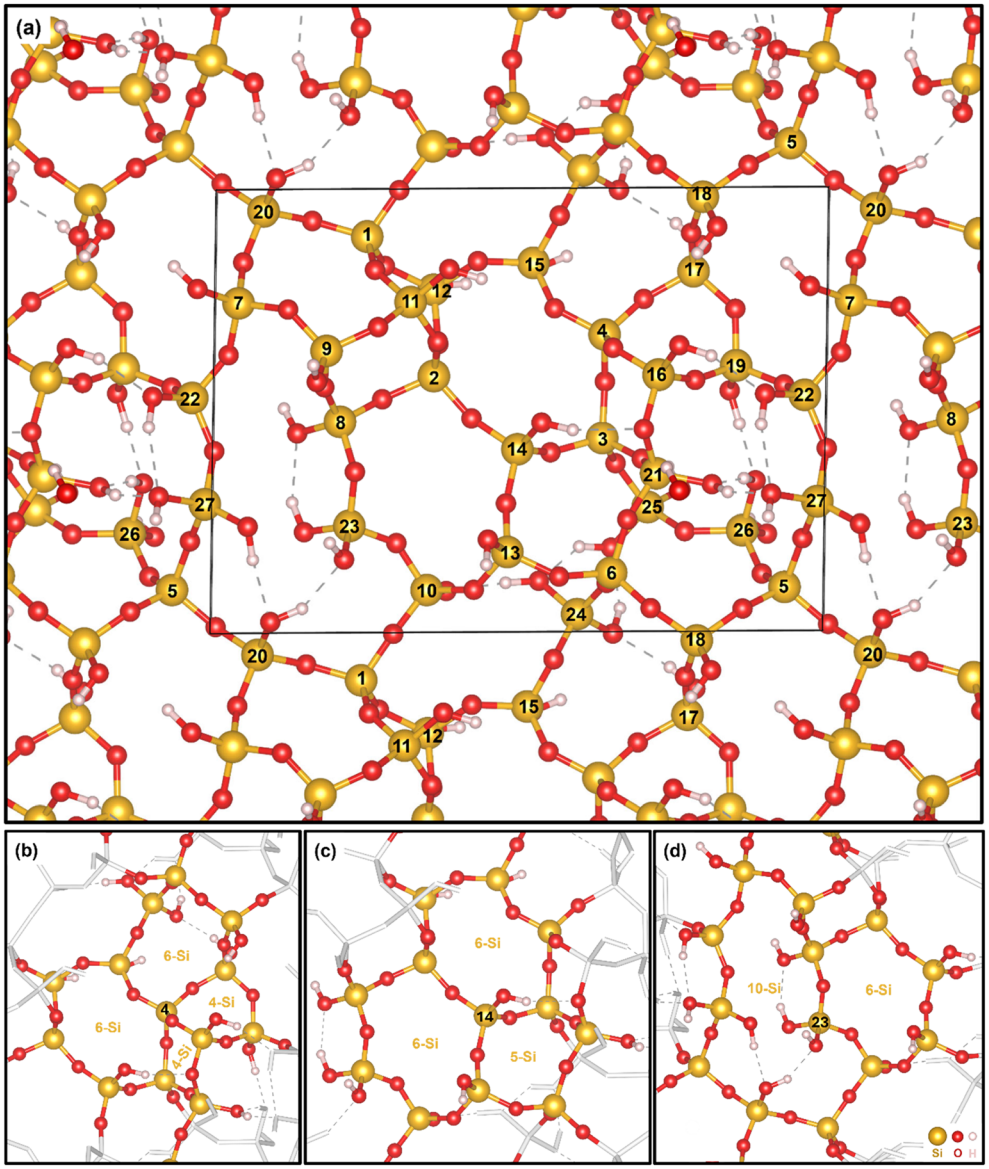

Fig. 2 (a) Representation of the periodicity of the unit cell of the amorphous silica model (centered area, top view). The model consists of silica rings varying from 4- to 10-membered Si rings (Fig. S3†), with a 4 : 2 : 3 : 2 : 1 : 1 : 1 : 1 distribution. It includes 6 $Si(O)_4$, 16 $Si(O)_3(OH)$, and 5 $Si(O)_2(OH)_2$ groups. The numbers indicate the 27 sites where $Ru^{(III)}$ can be located. In addition, $Ru^{(III)}$ can be grafted on the available silanol groups; (b) illustration of the four Si–O rings at site 4; (c) three Si–O rings at site 14, and (d) two Si–O rings at site 23.

sites were not explicitly modelled, but would correspond to some of the 21 silanol groups in the model.

Si-to-$Ru^{(III)}$ exchange involves replacing each Si site with $Ru^{(III)}$ and a TMP^+ (trimethylpropylammonium ion, $C_6H_{16}N^+$) or H^+ counterion to balance the charge ($\mathbf{R_1}$ and $\mathbf{R_2}$ in Fig. 4, respectively). This strategy allows to calculate the relative stability of $Ru^{(III)}$ at each of the 27 distinct sites within a common structural framework, thus enabling systematic comparison (Fig. S4†). To assess the role of the surfactant on the stability and activity of $Ru^{(III)}$ sites incorporated within amorphous silica, a TMP^+ molecule was positioned near the $Ru^{(III)}$ center to simulate the cetyltrimethylammonium surfactant ($C_{19}H_{42}N^+$, CTA^+) used experimentally. This activity and stability was compared with structures where H^+ was used as the counterion. H^+ was positioned at one of the oxygens adjacent to $Ru^{(III)}$. Depending on the type of oxygen (Ru–O–Si or Ru–OH), proton placement results in either the formation of a dative bond (Fig. 5a) or a H_2O molecule (Fig. 5b).

The flexible nature of the Si–O bonds facilitates the accommodation of $Ru^{(III)}$ in the amorphous silica walls, despite their different sizes and preferred geometries. Ruthenium is a larger atom, with an atomic radius of 134 pm, while silicon has an atomic radius of 111 pm. The tetrahedral geometry of $Si(OH)_4$ corresponds to O–Si–O angles of 109.5°, while in amorphous silica, the O–Si–O and Si–O–Si bond angles range between 102–119° and 130–180°, respectively.[9]

Molecular $Ru^{(III)}$ complexes prefer a square planar geometry (90° angles) when 4-coordinated, or an octahedral

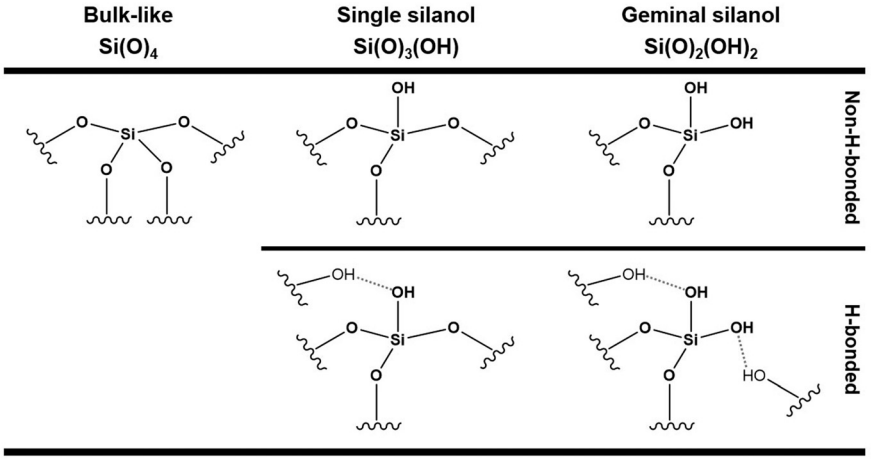

Fig. 3 Types of silica groups on the amorphous silica surface: $Si(O)_4$, $Si(O)_3(OH)$ and $Si(O)_2(OH)_2$. Hydrogen bonds in blue.

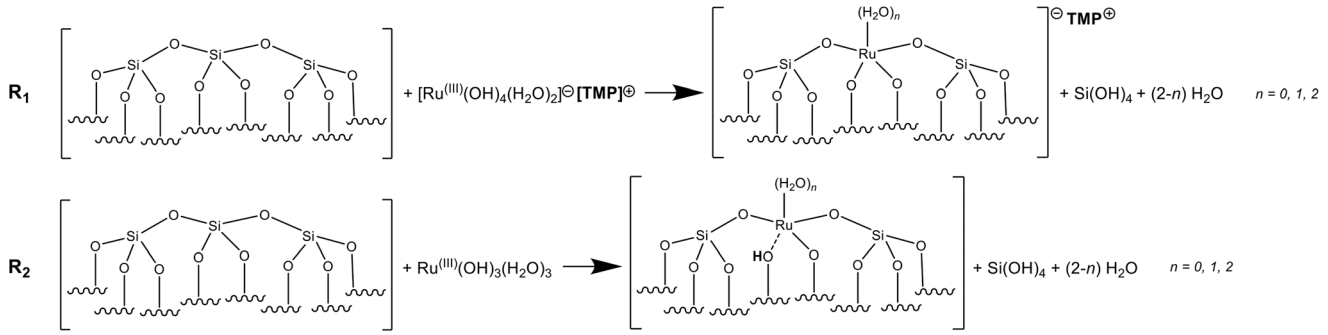

Fig. 4 Si-to-$Ru^{(III)}$ exchange reactions, in the presence of surfactant TMP^+ ($\mathbf{R_1}$) and with H^+ as counterion ($\mathbf{R_2}$). $Ru^{(III)}(O)_4$ as site example.

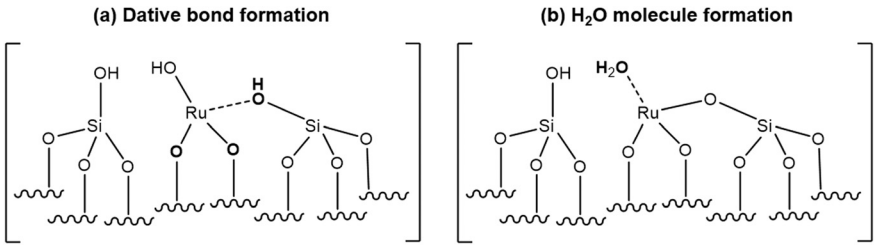

Fig. 5 (a) Formation of a dative bond (H^+ on Ru–O–Si), and (b) formation of a water molecule (H^+ on Ru–OH). $Ru^{(III)}(O)_3(OH)$ is used as a site example.

geometry when 6-coordinated.[35] In the amorphous silica structure, the preferred coordination number of $Ru^{(III)}$ was influenced by the flexibility around the exchanged Si site, varying between 4-coordinated (*i.e.*, bare $Ru^{(III)}$, without adsorbed water molecules) and 5- or 6-coordinated, with one or two adsorbed H_2O molecules, respectively.

3. Results and discussion

3.1. Molecular models for condensation of $Ru^{(III)}(OH)_3$ and $Si(OH)_4$

Before evaluating the stability and activity of various possible $Ru^{(III)}$ sites in amorphous silica, we first study the condensation reactions for model $Ru^{(III)}$ species, such as $Ru(OH)_3$, $[Ru(OH)_4]^-$, $[Ru(OH)_4]^-[TMP]^+$ with $Si(OH)_4$ to better understand factors governing the Si–O–Ru bond strength. We also benchmark the PBE-D3(BJ) calculations against reference DLPNO-CCSD(T)/Def2-TZVP for these molecular models (Table 1).

The condensation of two orthosilicic acid molecules ($Si(OH)_4$) into pyrosilicic acid ($(OH)_3SiOSi(OH)_3$) to model the formation of a siloxane (Si–O–Si) bridge was calculated in reaction $\mathbf{R_3}$. Condensation is energetically favorable and well described by PBE-D3(BJ). Condensation of $Ru^{(III)}(OH)_3$ with $Si(OH)_4$, is slightly less energetically favorable ($\mathbf{R_4}$), but becomes more energetically favorable when octahedral $Ru^{(III)}(OH)_3(H_2O)_3$ condenses ($\mathbf{R_5}$). Interestingly, condensation becomes significantly more favorable for $[Ru^{(III)}(OH)_4]^-[TMP]^+$

Table 1 Condensation and water adsorption energies calculated with PBE-D3(BJ) and DLPNO-CCSD(T)/Def2-TZVP[a] methods. ΔE_{Elect} values in kJ mol^{-1}

Condensation and water adsorption reactions		PBE-D3(BJ) (VASP)	DLPNO-CCSD(T)/Def2-TZVP[a]
$\mathbf{R_3}$	$2Si(OH)_4 \rightarrow (OH)_3SiOSi(OH)_3 + H_2O$	−57	−52
$\mathbf{R_4}$	$Si(OH)_4 + Ru(OH)_3 \rightarrow (OH)_3SiORu(OH)_2 + H_2O$	−38	−25
$\mathbf{R_5}$	$Si(OH)_4 + Ru(OH)_3(H_2O)_3 \rightarrow (OH)_3SiORu(OH)_2(H_2O)_3 + H_2O$	−61	−67
$\mathbf{R_6}$	$Si(OH)_4 + [Ru(OH)_4]^-[TMP]^+ \rightarrow [(OH)_3SiORu(OH)_3]^-[TMP]^+ + H_2O$	−110	−102
$\mathbf{R_7}$	$Si(OH)_4 + [Ru(OH)_4(H_2O)_2]^-[TMP]^+ \rightarrow [(OH)_3SiORu(OH)_3(H_2O)_2]^-[TMP]^+ + H_2O$	−104	−109
$\mathbf{R_8}$	$Si(OH)_4 + [Ru(OH)_4]^- \rightarrow [(OH)_3SiORu(OH)_3]^- + H_2O$	−134[b]	−137
$\mathbf{R_9}$	$Si(OH)_4 + [Ru(OH)_4(H_2O)_2]^- \rightarrow [(OH)_3SiORu(OH)_3(H_2O)_2]^- + H_2O$	−118[b]	−123
$\mathbf{R_{10}}$	$Ru(OH)_3 + 3\ H_2O \rightarrow Ru(OH)_3(H_2O)_3$	−92	−109
$\mathbf{R_{11}}$	$[Ru(OH)_4]^-[TMP]^+ + 2\ H_2O \rightarrow [Ru(OH)_4(H_2O)_2]^-[TMP]^+$	−63	−128
$\mathbf{R_{12}}$	$[Ru(OH)_4]^- + 2\ H_2O \rightarrow [Ru(OH)_4(H_2O)_2]^-$	−68[b]	−109

Ruthenium is present in its $Ru^{(III)}$ oxidation state in all reactions. [a] Geometry optimizations with PBE-D3(BJ)/Def2-TZVP, followed by single-point calculations using DLPNO-CCSD(T)/Def2-TZVP. [b] PBE-D3(BJ)/Def2-TZVP calculations for charged species using ORCA.

($\mathbf{R_6}$), pointing toward the role of the surfactant in stabilizing the $Ru^{(III)}$ active sites within the amorphous silica framework. This enhanced stability was also calculated for the condensation with $[Ru^{(III)}(OH)_4]^-$ ($\mathbf{R_8}$). In general, PBE-D3(BJ) calculations agree well with the high-level DLPNO-CCSD(T)/Def2-TZVP. Both methodologies reliably describe Si–O–Si and Si–O–Ru bonds, supporting the applicability of PBE-D3(BJ) for studying the incorporation of $Ru^{(III)}$ in amorphous silica.

Water adsorption is energetically favorable on $Ru^{(III)}(OH)_3$ ($\mathbf{R_{10}}$), $[Ru^{(III)}(OH)_4]^-[TMP]^+$ ($\mathbf{R_{11}}$) and $[Ru^{(III)}(OH)_4]^-$ ($\mathbf{R_{12}}$), in line with the preferred octahedral coordination of $Ru^{(III)}$. The calculated adsorption energy is approximately 30 kJ mol^{-1} per H_2O molecule. DLPNO-CCSD(T)/Def2-TZVP calculations suggest that PBE-D3(BJ) slightly underestimates H_2O adsorption. Since water desorption is an important step in the formation of $Ru^{(III)}$-hydride species, PBE-D3(BJ) calculations might slightly overestimate the stability of the hydride relative to the hydrated $Ru^{(III)}$ reactant state.

3.2. Stability of $Ru^{(III)}$ sites

The amorphous silica model offers 27 potential sites for $Ru^{(III)}$ incorporation and 21 silanol groups where $Ru^{(III)}$ can be grafted. Si-to-$Ru^{(III)}$ exchange energies were calculated according to reactions $\mathbf{R_1}$ and $\mathbf{R_2}$ (Fig. 4) and are presented in Fig. 6. $Ru^{(III)}(O)_4$, $Ru^{(III)}(O)_3(OH)$ and $Ru^{(III)}(O)_2(OH)_2$ are represented by sites 1–6, sites 7–22, and sites 23–27, respectively.

The incorporation of $Ru^{(III)}$ into amorphous silica is highly favorable, with Si-to-$Ru^{(III)}$ exchange energies ranging from −25 to −248 kJ mol^{-1} in the presence of TMP^+. In the absence of surfactant, the exchange energies shift to a range of +24 to −118 kJ mol^{-1}, indicating the evident stabilization effect provided by the surfactant. Also for the molecular complexes, the exchange energy is −53 kJ mol^{-1} for $[Ru^{(III)}(OH)_4]^-[TMP]^+$ ($\mathbf{R_6}$ and $\mathbf{R_3}$, Table 1) and only −4 kJ mol^{-1} for $Ru^{(III)}(OH)_3(H_2O)_3$ ($\mathbf{R_5}$ and $\mathbf{R_3}$, Table 1) per Si–O–Ru bond formed. Note that only a single Si–O–Ru bond is formed in the molecular complexes, and so the molecular energies are lower than the values in Fig. 6. The wide variation in exchange energies in the amorphous silica indicates that multiple factors, such as the size of the silica rings, the coordination environment and the hydrogen bonding interactions, affect the stability of $Ru^{(III)}$ sites.

To isolate effects associated with the amorphous silica structure from stabilization by adsorption of H_2O molecules, we first analyze the stability of bare $Ru^{(III)}$ sites (without adsorbed H_2O molecules) in the presence of surfactant TMP^+.

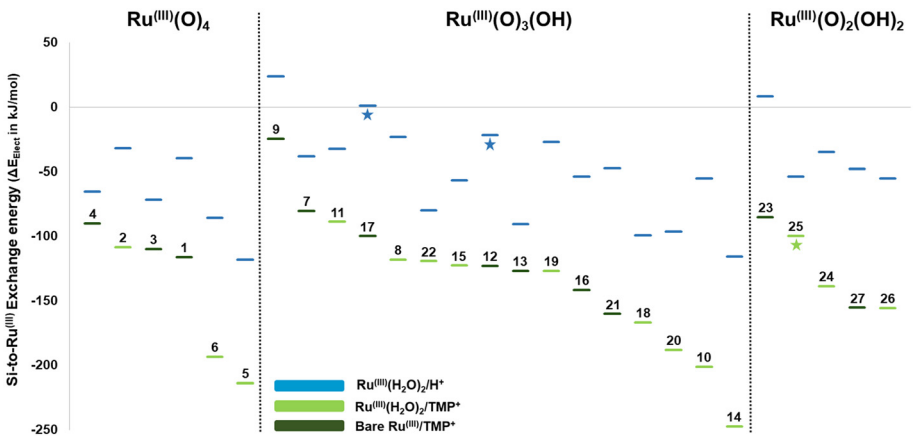

Fig. 6 Si-to-$Ru^{(III)}$ exchange energy diagram, in the presence ($Ru^{(III)}$/TMP^+, in green) and in the absence of surfactant ($Ru^{(III)}$/H^+, in blue). Energies calculated according to reactions $\mathbf{R_1}$ (with TMP^+) and $\mathbf{R_2}$ (with H^+), using $Ru^{(III)}(O)_4$ as site example. Bare $Ru^{(III)}$ sites denote sites without adsorbed H_2O molecules and the star icon indicate sites with only one adsorbed H_2O molecule. Groups are ordered by increasing stability, in reference to $Ru^{(III)}$/TMP^+ sites. DFT calculations were performed with PBE-D3(BJ) and electronic energies are in kJ mol^{-1}.

Table 2 Size of the silica rings for each $Ru^{(III)}$ site, and the corresponding Si-to-$Ru^{(III)}$ exchange energy for bare $Ru^{(III)}$ sites, in the presence of TMP^+. The sites are listed in order of increasing stability according to the type of Si group

Type of site	Site	Ring sizes (number of Si atoms)	Si-to-$Ru^{(III)}$ exchange energy[a] (kJ mol^{-1})
$Si(O)_4$	2	4, 4, 6, 6	−72
	4	4, 4, 6, 6	−90
	3	4, 5, 6, 9	−110
	1	4, 5, 7, 10	−116
	6	5, 6, 7, 8	−169
	5	7, 7, 8, 10	−172
$Si(O)_3(OH)$	9	4, 5, 10	−25
	11	4, 4, 5	−53
	8	4, 6, 10	−70
	7	5, 7, 10	−80
	19	4, 7, 8	−87
	17	4, 6, 7	−89
	22	7, 8, 10	−102
	15	6, 6, 7	−108
	12	4, 6, 7	−123
	13	5, 6, 7	−127
	10	6, 7, 10	−141
	16	4, 4, 8	−142
	21	4, 5, 8	−160
	18	6, 7, 8	−163
	14	5, 6, 6	−183
	20	5, 7, 10	−190
$Si(O)_2(OH)_2$	25	8, 9	−40
	23	6, 10	−85
	26	8, 9	−115
	24	6, 7	−139
	27	8, 10	−155

[a] Si-to-$Ru^{(III)}$ exchange energy calculated according to reaction $\mathbf{R_1}$ in Fig. 4, with $n = 0$ (no adsorbed H_2O molecules).

Table 2 summarizes the number of Si-membered rings and their respective size for each site (number of Si atoms per ring), along with the corresponding Si-to-$Ru^{(III)}$ exchange energy.

Exchanging tetrahedral Si with square planar $Ru^{(III)}$ induces deformation in the silica structure. The extent of this deformation depends on factors such as the ring strain at each site. The effect of ring strain is quite pronounced for bulk-like $Si(O)_4$ sites, with stability predominantly influenced by the size of the involving silica rings. This distinction is evident when comparing sites 1–4 (comprising small Si rings) to sites 5–6 (featuring larger Si rings). sites 1–4 are characterized by one or two 4-membered Si rings, with the lowest stability observed at sites which are part of two 4-membered Si rings (sites 2 and 4). For example, while both sites 2 and 5 exhibit $Ru^{(III)}$ adopting a square planar geometry, this configuration affects the two sites differently. At site 2, the local ring geometry is significantly distorted to accommodate $Ru^{(III)}$ (Fig. 7a). This distortion is reflected in the bond angles, where the change in Si–O–Si to Si–O–Ru is evident. Although some bond angles, such as $\measuredangle_3$ and $\measuredangle_6$ (163° and 161°, respectively), shift closer to the typical Si–O–Si bond angle of 140°, the replacement of a tetrahedral Si with a square planar $Ru^{(III)}$ significantly alters the local geometry. Despite some bond angles adjusting to the new structure, the exchange is not completely optimal due to the strain caused by the distinct geometry and atomic size.

The larger rings surrounding site 5 allow $Ru^{(III)}$ to adopt a square planar geometry with significantly less strain (Fig. 7b), resulting in a 100 kJ mol^{-1} stability gain for site 5 compared to site 2. The structural changes that occur upon the exchange of a Si site for $Ru^{(III)}$ are as expected. Specifically, the distance between opposing oxygen atoms (O1–O3, O2–O4 in Fig. 7b) increases when $Ru^{(III)}$ is incorporated, from approximately 2.70 Å to 3.85 Å. This leads to the silica rings either opening up or changing their structure to accommodate the larger $Ru^{(III)}$ atom. Despite these changes in the local geometry, the energies associated with the Si-to-$Ru^{(III)}$ exchange are not much influenced by these structural adjustments.

For $Ru^{(III)}(O)_3(OH)$ and $Ru^{(III)}(O)_2(OH)_2$ sites, it becomes more challenging to pinpoint the main factors affecting their stability. Ring strain and hydrogen bonding play key roles in determining the stability for $Ru^{(III)}(O)_3(OH)$ groups, but this strongly depends on the geometry of the site. Sites 7 and 20 are examples of the impact of ring strain. Both sites are part of the same Si–O ring system (5-,7- and 10-membered Si rings) and achieve square planar geometry, but their stabilities differs by 110 kJ mol^{-1} (Fig. 8). At first glance, site 7 would be expected to be very stable due to its nearly ideal O–Ru–O angles (close to 90°) and the seemingly sufficient space to adopt the preferred geometry (Fig. 8b). Additionally, $Ru^{(III)}$ incorporation at site 7 leads to the formation of extra hydrogen bonds compared to the initial amorphous slab. Surprisingly, site 7 is one of the least stable sites. This instability arises because the incorporation of $Ru^{(III)}$ causes

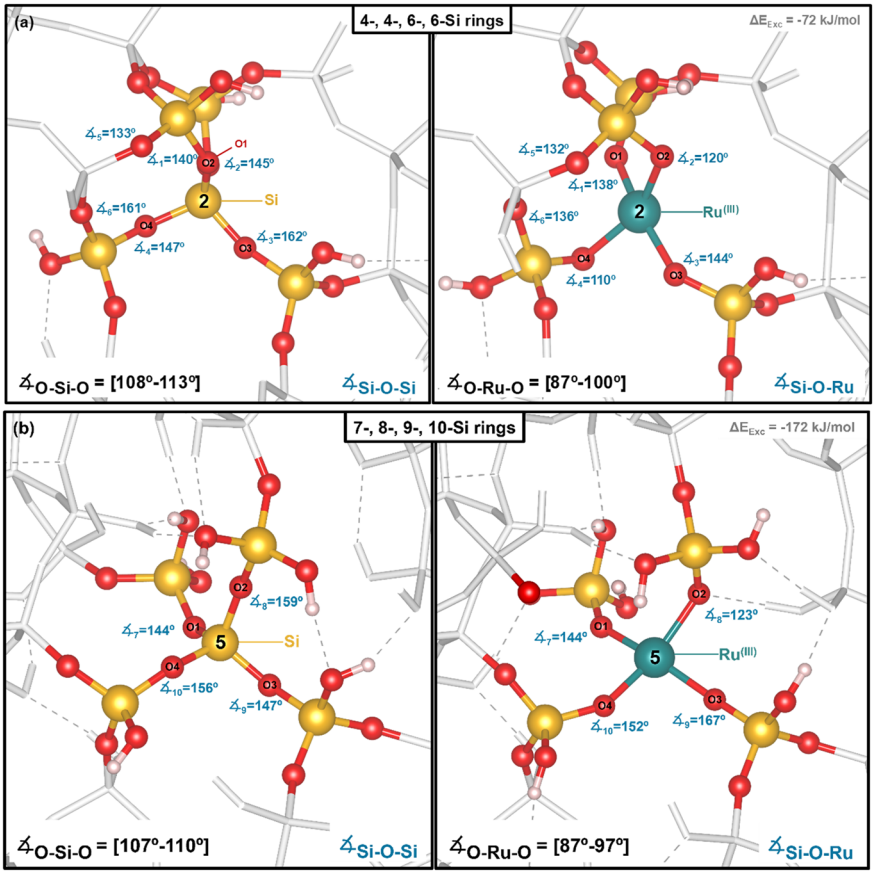

Fig. 7 Bond angles in the Si slab (Si–O–Si and O–Si–O) are shown on the left, and the bond angles for the bare $Ru^{(III)}$ in the presence of TMP^+ (Si–O–Ru and O–Ru–O) are shown on the right for (a) site 2 and (b) site 5. TMP^+ molecule not shown in the figures.

significant distortion of the Si–O–Si angles in the nearby 4-membered Si ring (highlighted in Fig. 8b) to accommodate the square planar geometry—particularly a sharp change in the $\measuredangle_6$ angle. Similar to site 2, the angles become similar in value to others, but this change introduces strain into the structure, causing a less favorable Si-to-$Ru^{(III)}$ exchange. This shows that the strain effect is not confined to the site itself but can propagate as a ripple effect throughout the amorphous structure. Site 20 offers sufficient space for $Ru^{(III)}$ to adopt a square planar arrangement with minimal structural changes (Fig. 8c), resulting in substantially higher stability than site 7.

Small-membered rings are not always directly correlated with instability. For example, sites 16 and 21 belong to 4-membered Si rings but are part of the most stable structures for the $Ru^{(III)}(O)_3(OH)$ group (Fig. 8e and f). Both sites achieve optimal square planar geometry, and the observed distortion of the rings is consistent with what would be expected after replacing a Si atom by a $Ru^{(III)}$ atom. Hydrogen bonding also contributes to the stabilization of these sites by preserving the number of hydrogen bonds from the initial amorphous structure. The incorporation of $Ru^{(III)}$ at Sites 16 and 21 does not significantly disrupt the hydrogen bonding network established in the amorphous silica structure, further enhancing their stability.

When comparing the stability of $Ru^{(III)}$ sites located in the 4-membered Si rings, it is evident that the strain induced by these rings also varies. The strain in the 4-Si rings containing Sites 2 and 4 is much more pronounced than that in the 4-Si rings containing sites 16 and 21. This indicated that the structural configuration of these rings also influences the level of strain, and not necessarily just their size (number of Si atoms).

$Ru^{(III)}(O)_2(OH)_2$ groups can benefit significantly from hydrogen bonding interactions particularly because of their proximity to highly hydroxylated regions in the amorphous structure. These groups tend to easily adopt a square planar geometry due to their position within larger Si rings and the flexibility provided by the two hydroxyl groups. This flexibility allows them to form hydrogen bonds, which enhance their stability. For example, sites 23 and 27 are located within the same 10-membered Si ring and have similar O–Ru–O angles ([89–92°] and [86–95°], respectively), but the position of site 27 facilitates the formation of hydrogen bonds, resulting in a stabilization effect of 70 kJ mol^{-1}. While this flexibility makes Si-to-$Ru^{(III)}$ exchange favorable for $Ru^{(III)}(O)_2(OH)_2$ groups, their stability is limited by the formation of only two Si–O–Ru bonds. Molecular calculations reveal that condensation of $[Ru^{(III)}(OH)_4]^-[TMP]^+$ with $Si(OH)_4$ is energetically more favorable than self-condensation of $Si(OH)_4$, favoring the

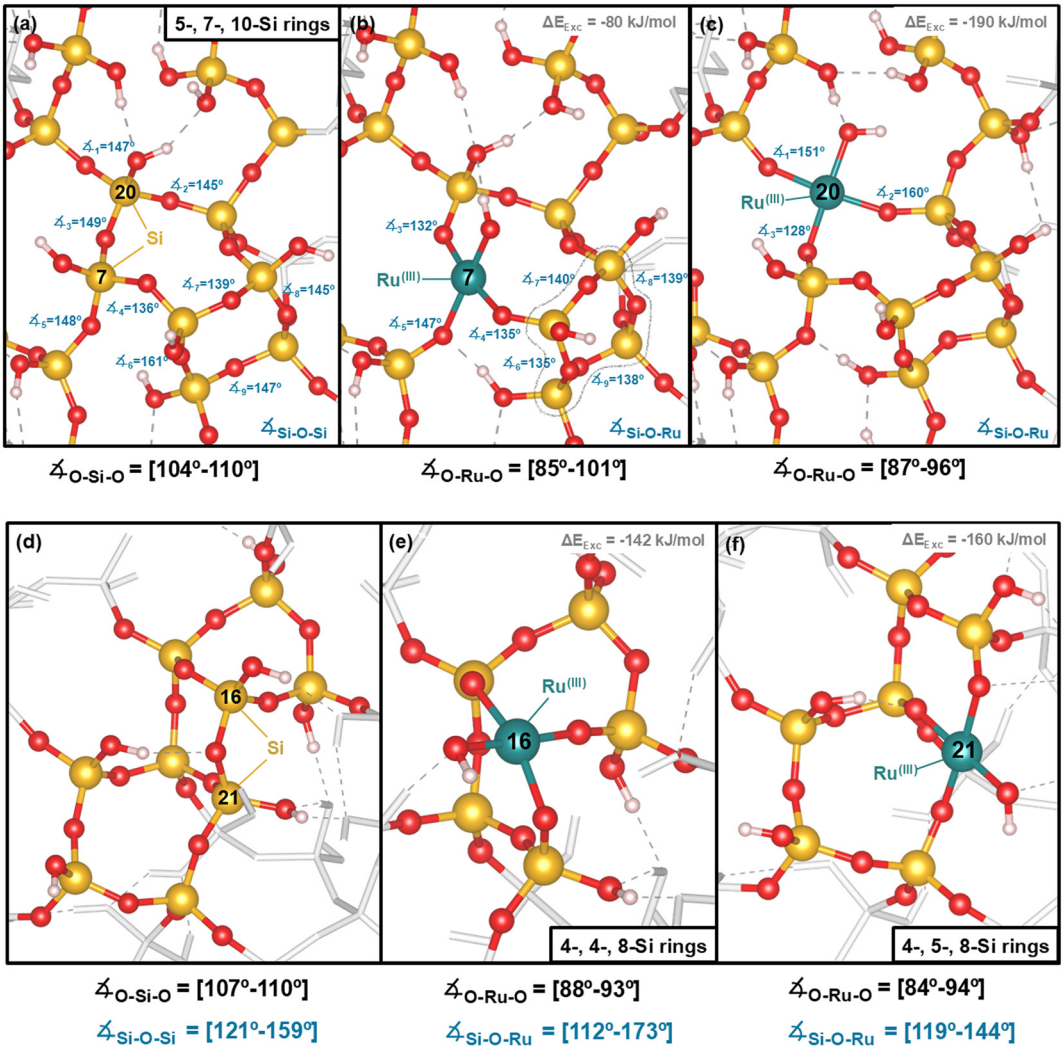

Fig. 8 Silica slab highlighting (a) sites 7 and 20 and (d) sites 16 and 21, and the relevant Si–O–Si and O–Si–O bond angles; incorporation of bare $Ru^{(III)}$/TMP^+ (b) in site 7, (c) in site 20, (e) in site 16 and (f) in site 21, and the respective Si–O–Ru and O–Ru–O bond angles. TMP^+ molecule not shown in the figures.

formation of multiple Si–O–Ru bonds, and thus favoring the formation of $Ru^{(III)}(O)_4$ sites, whenever possible.

3.2.1. H_2O adsorption. The preferred octahedral coordination sphere of $Ru^{(III)}$ can be completed by adsorption of two H_2O molecules, if space permits. According to Table 1, water adsorption on $[Ru^{(III)}(OH)_4]^-[TMP]^+$ is favorable, with an energy gain of 32 kJ mol^{-1} per H_2O molecule (reaction $\mathbf{R_{11}}$). However, within the amorphous silica structure, the coordination of water may be hindered by steric repulsion and may disrupt the existing hydrogen bonding network. The Si-to-$Ru^{(III)}$ exchange energy diagram in Fig. 6 highlights the sites where water adsorption on $Ru^{(III)}$ is beneficial.

Sites located within larger Si rings, such as sites 5, 10 and 14, significantly facilitate adsorption of water, enhancing the stability of these $Ru^{(III)}$ sites. Interestingly, sites 9 and 18, despite being located within smaller rings, also benefit from water adsorption. In contrast, 6-coordinated $Ru^{(III)}$ at sites 3 and 16 does not represent the most stable configuration. The deformation of the octahedral geometry caused by steric repulsion results in substantial energy penalties of +94 and +116 kJ mol^{-1}, respectively, when compared to the bare $Ru^{(III)}$ sites (no adsorbed H_2O molecules) (Fig. 9 and Table S4†).

Certain sites, such as site 4, lack sufficient space for H_2O adsorption, while at other positions, adsorbed water molecules desorb to interact with nearby silanol groups (*e.g.*, site 27).

Water adsorption complicates the analysis of the stabilities of $Ru^{(III)}$ incorporated into amorphous silica. While $Ru^{(III)}$ prefers to adopt an octahedral geometry, the local geometry of each site ultimately dictates its stabilities. Our analysis demonstrates that the model used to represent $Ru^{(III)}$@MCM-41 captures the heterogeneity of potential $Ru^{(III)}$ sites, consistent with what is expected in a real amorphous silica structure.

Based on the Si-to-$Ru^{(III)}$ exchange energies in the presence of surfactant, it is likely that $Ru^{(III)}$ is incorporated

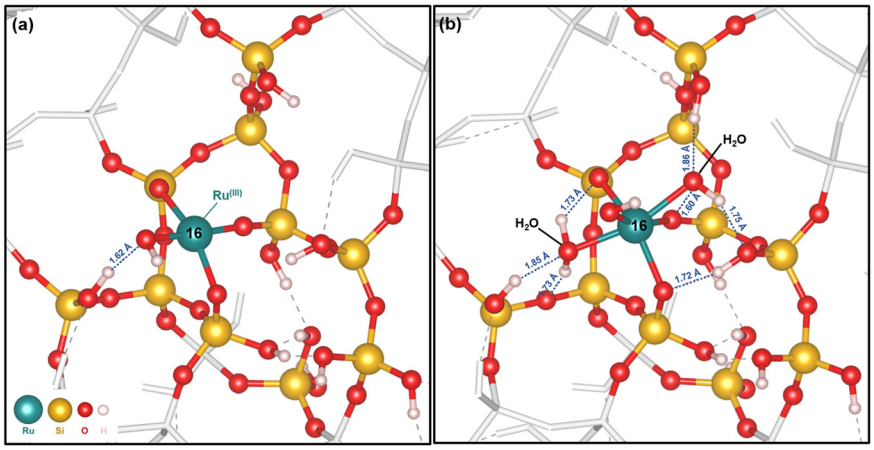

Fig. 9 Incorporation of $Ru^{(III)}$ at site 16, in the presence of surfactant: (a) bare $Ru^{(III)}$, and (b) with two adsorbed H_2O molecules (indicated in the figure). Blue lines represent the hydrogen bond interactions around the $Ru^{(III)}$ center and their respective distances (in Å). TMP^+ molecule not shown in the figure.

as $Ru^{(III)}(O)_4$ and $Ru^{(III)}(O)_3(OH)$ groups, accompanied by two adsorbed water molecules. This aligns with the energetically favorable condensation of $Ru^{(III)}$ to form multiple Si–O–Ru bonds.

Potential sites for $Ru^{(III)}$ include sites 5, 6, 10, 14 or 20 (Fig. 6). These sites are located within larger Si rings, where ring strain is less pronounced, allowing the substitution of tetrahedral Si with a larger octahedral $Ru^{(III)}$ without causing significant structural changes. For $Ru^{(III)}(O)_3(OH)$ sites, the flexibility provided by the OH group allows $Ru^{(III)}$ to more easily adopt a square planar geometry. Octahedral coordination is achieved through favorable adsorption of two H_2O molecules, facilitated by the available space at these sites and the presence of hydrogen-bonding interactions.

3.2.2. Hydrolysis of $Ru^{(III)}$ sites. Wang *et al.*[27] reported that $Ru^{(III)}$ single sites in solid micellar catalysts can reversibly switch to Ru^0 nanoclusters and back in the presence of both water and hydrogen.

The formation of these Ru^0 nanoclusters is suggested to occur *via* the hydrolysis of Si–O–Ru bonds, leading to the formation of $Ru^{(III)}(OH)_3(H_2O)_3$ complexes, followed by condensation and reduction of these $Ru^{(III)}(OH)_3(H_2O)_3$ complexes, which drives the interconversion. After hydrolysis, the surfactant remains near the amorphous silica wall, interacting with the newly formed silanoxo ($[Si–O]^-[TMP]^+$) group.

To evaluate the stability of the $Ru^{(III)}$ single-sites in the amorphous silica, we computed hydrolysis energies for sites 5, 6, 10, 14 and 20 (Table S6,† and part III. Hydrolysis of $Ru^{(III)}$ sites in the ESI†). Hydrolysis is unfavorable for all five sites. Interestingly, hydrolysis of $Ru^{(III)}(O)_4(H_2O)_2$ sites (+28 kJ mol^{-1} for site 5 and +48 kJ mol^{-1} for site 6) is less unfavorable that hydrolysis of $Ru^{(III)}(O)_3(OH)(H_2O)_2$ sites (+81 kJ mol^{-1} for site 20, +148 kJ mol^{-1} for site 10 and +153 kJ mol^{-1} for site 14, Table S6†).

Hydrolysis differs from the exchange reactions and is strongly influenced by the stability of the resulting silanoxo group (see Fig. S5†). Hydrogen bonding at silanoxo groups resulting from $Ru^{(III)}(O)_4$ hydrolysis explains the lower hydrolysis energies for sites 5 and 6.

3.2.3. Two $Ru^{(III)}$ sites per unit cell. A typical $Ru^{(III)}$@MCM-41 catalyst with 3.1 wt% $Ru^{(III)}$ has a Si/$Ru^{(III)}$ ratio of about 15. This translates into about two $Ru^{(III)}$ sites per unit cell in our model. To explore how the relative positioning of these $Ru^{(III)}$ sites influences their stability, we evaluated pairs of the most stable $Ru^{(III)}$ sites – namely sites 5, 6, 10, 14, and 20. These calculations were performed considering bare $Ru^{(III)}$ sites (no adsorbed H_2O molecules).

The Si-to-$Ru^{(III)}$ exchange energies for the different pairs are compared with the sum of the individual exchange energies (one $Ru^{(III)}$ per unit cell, Table 2) in Fig. S6† (in kJ mol^{-1} of $Ru^{(III)}$). In most cases, the incorporation of two $Ru^{(III)}$ sites in the unit cell slightly decreases the stability (up to +24 kJ mol^{-1}). Pairs that include site 14 are more destabilized (up to +50 kJ mol^{-1}). In some cases, the pairs are slightly more stable than the isolated $Ru^{(III)}$ sites. The flexibility of the amorphous silica seems to accommodate the introduction of two $Ru^{(III)}$ sites without restricting their ability to adopt their preferred square planar geometry. It is even favorable for two $Ru^{(III)}$ sites to be located adjacent to each other, as observed for the pair of sites 5 and 20 (Fig. 10). Similarly, $Ru^{(III)}$ sites located within the same rings (*e.g.*, sites 6 and 10) do not pose structural constraints.

3.2.4. Grafted $Ru^{(III)}$ sites. To explore additional site environments that may exist at the surface of the amorphous silica pore walls, we also considered the possibility of $Ru^{(III)}$ sites forming through condensation with silanol groups located at the surface of the amorphous silica model. These sites, referred to as grafted $Ru^{(III)}$ sites, are formed by the reaction of two, three, or four silanol groups with $[Ru^{(III)}(OH)_4(H_2O)_2]^-[TMP]^+$ ($\mathbf{R_{13}}$) to form grafted $Ru^{(III)}(O)_2(OH)_2$, $Ru^{(III)}(O)_3(OH)$ and $Ru^{(III)}(O)_4$ sites, respectively.

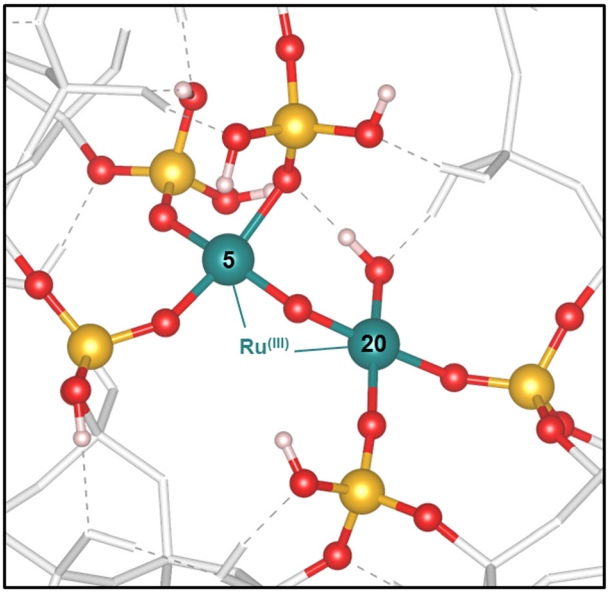

Fig. 10 Two $Ru^{(III)}$ sites located adjacent to each other at sites 5 and 20 (no adsorbed H_2O molecules). TMP^+ molecules not shown in the figure.

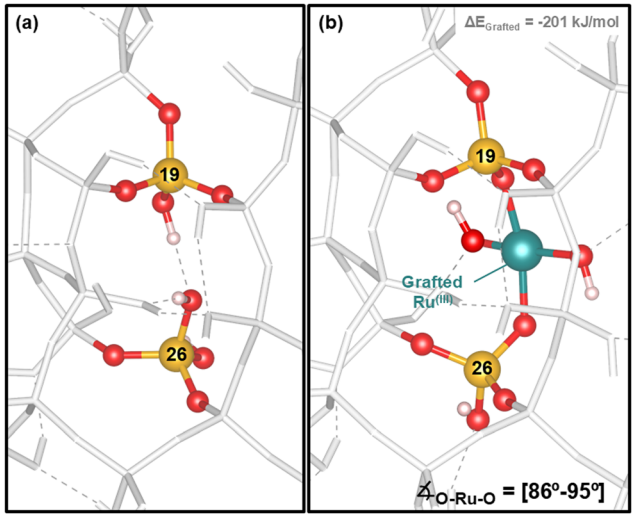

Fig. 11 (a) Si slab model highlighting sites 19 and 26; (b) $Ru^{(III)}(O)_2(OH)_2(H_2O)_2$ site result of the $Ru^{(III)}$ grafting at the two silanoxo groups at sites 19–26. TMP^+ molecule not shown in the figure.

$$\mathbf{R_{13}}\quad Si_{27}O_{41}(OH)_{26}+\left[Ru^{(III)}(OH)_4(H_2O)_2\right]^-[TMP]^+ \rightarrow \left[Si_{27}O_{41}(OH)_{26-x}\left(Ru^{(III)}(O)_x(OH)_{4-x}(H_2O)_y\right)\right]^-[TMP]^+ + (2+x-y)H_2O \quad x=2,\ 3,\ 4 \text{ and } y=0,\ 1,\ 2$$

The grafting energies range from +49 to −240 kJ mol^{-1} per grafted $Ru^{(III)}$ (Fig. S7†). Grafting energies cannot be directly compared to exchange energies since the involved reactions are very different and use a different silica reference (Fig. S4†). To make a direct and meaningful comparison, the stability of $Si(OH)_4$, formed in the Si-to-$Ru^{(III)}$ exchange reaction, needs to be accounted for. One way could be to subtract the hydrolysis energy of the complete silica slab, corresponding to +80 kJ mol^{-1} per $Si(OH)_4$ (calculated *via* $\mathbf{R_{S2}}$) from the grafting energies.

Multiple grafted $Ru^{(III)}(O)_2(OH)_2$ and $Ru^{(III)}(O)_3(OH)$ sites can form on the silica slab model. The flexibility of Si–O bonds, combined with an optimal distance between silanoxo groups, facilitated grafting of $Ru^{(III)}$ and allowed it to achieve its preferred square planar geometry. Although condensation with silanol groups in highly hydroxylated areas disrupts the local hydrogen-bonding network, for example at sites such as sites 19–26 (Fig. 11), the incorporation of $Ru^{(III)}$ allowed for interactions with neighboring hydroxyl groups, enhancing stability.

Formation of grafted $Ru^{(III)}(O)_4$ species proved to be more difficult, as only a limited number of stable configurations could be identified. Hydroxylated regions were found to contain sites with four nearby silanoxo groups, but the confined space in these regions prevented $Ru^{(III)}$ from adopting a square planar geometry. This spatial constraint is a significant factor contributing to the instability of grafted $Ru^{(III)}(O)_4$ species.

Based on molecular complex calculations, $Ru^{(III)}(O)_4$ groups would be expected to exhibit greater stability (Table 1). However, the structural limitations imposed by the amorphous silica framework reveal the influence of these constraints. As a result, the formation of grafted $Ru^{(III)}(O)_2(OH)_2$ species is favored over the more highly condensed grafted $Ru^{(III)}(O)_4$ sites.

The grafting of $Ru^{(III)}$ sites onto adjacent silanol groups ($(OH)(O)_2Si–O–Si(O)_2(OH)$) was energetically unfavorable. For instance, grafting $Ru^{(III)}$ at the silanol groups at sites 10–15–24 and sites 9–11 (Fig. S8†) leads to the formation of very small rings with two-membered Si atoms, resulting in grafting energies of +26 and +17 kJ mol^{-1}, respectively.

Water adsorption proved difficult for most grafted structures due to spatial limitations imposed by structural constraints. Even at sites where sufficient space allowed the coordination of one H_2O molecule and $Ru^{(III)}$ adopting a 5-coordinated geometry, the H_2O molecule often desorbed. As a result, only a very limited number of grafted $Ru^{(III)}$ sites allowed favorable water adsorption. Grafting of $Ru^{(III)}$ mostly results in $Ru^{(III)}(O)_2(OH)_2$ sites (both bare and with two adsorbed H_2O molecules) and, to a lesser extent, in octahedral $Ru^{(III)}(O)_3(OH)(H_2O)_2$ sites (Fig. S7†).

3.3. Counterion exchange: TMP^+ to H^+

To investigate the role of the surfactant in stabilizing the $Ru^{(III)}$ sites in amorphous silica, the counterion TMP^+ was replaced by a proton (H^+), simulating a surfactant-free environment. This

substitution alters the nature of the interaction of the oxygen atom with $Ru^{(III)}$, and leads to the formation of either a dative bond (Fig. 5a) or a water molecule (Fig. 5b).

Si-to-$Ru^{(III)}$ exchange energies for the bare sites with H^+ as the counterion are significantly less favorable than those calculated in the presence of TMP^+ (Fig. 6 and Table S7†). Water adsorption again plays a crucial role in stabilizing these $Ru^{(III)}$ sites, contributing to an energy gain ranging from −23 to −156 kJ mol^{-1}. This is consistent with the water adsorption effect calculated for the molecular complexes (Table 1). In many of the sites, substantial structural changes occur to accommodate the adsorbed water molecules.

The factors influencing site stability remain similar to those identified in the presence of the surfactant. Ring strain continues to significantly impact the stability of $Ru^{(III)}(O)_4$ sites, and the introduction of H^+ allows for strain relief through the formation of dative bonds (*e.g.*, site 4). In larger rings, such as sites 5 and 6, dative bonds remained near the $Ru^{(III)}$ center to complete the octahedral coordination. The preferred position of the proton at $Ru^{(III)}(O)_3(OH)$ and $Ru^{(III)}(O)_2(OH)_2$ sites shows more variability, with preference for either water or dative bond formation depending on the local structure environment.

The Si-to-$Ru^{(III)}$ exchange energy diagram in Fig. 6 highlights the stabilizing role of the surfactant. Some sites show a stability gain of more than 100 kJ mol^{-1} in the presence of the TMP^+ (*e.g.*, sites 6, 10, 14 and 26), with minimal structural changes.

With H^+ as the counterion, $Ru^{(III)}$ is again most likely incorporated in $Ru^{(III)}(O)_4$ or $Ru^{(III)}(O)_3(OH)$ sites, with two adsorbed H_2O molecules. The calculated formation energies of $Ru^{(III)}(O)_2(OH)_2$ sites indicate that this configuration is energetically less favorable.

3.4. Formation of $Ru^{(III)}$-hydride species

Hydrogen activation is a key step in hydrogenation reactions.[36] In $Ru^{(III)}$@MCM-41, H_2 activation occurs through heterolytic dissociation with no change in the formal oxidation state of the $Ru^{(III)}$ center, leading to the formation of a $Ru^{(III)}$-hydride and of a H_2O molecule or a dative bond (Fig. 12),[25,26] after which the proton may migrate to another base site, such as silanoxo groups.

The formation energies of $Ru^{(III)}$-hydride species were calculated for all 27 exchanged $Ru^{(III)}$ sites. In the presence of the surfactant, hydride formation is favorable, with values ranging from +21 to −113 kJ mol^{-1} (Fig. 13). Without the surfactant (with H^+ as the counterion), hydride formation remains favorable, but to a lesser extent (Fig. S10†). This highlights the significant stabilizing effect of TMP^+ also on the formation of the $Ru^{(III)}$-hydride species. These findings also align with calculations for molecular complexes (Table 3); hydride formation is significantly more favorable for $[Ru^{(III)}(OH)_4]^-[TMP]^+$ (**R**$_{18}$) and $[Ru^{(III)}(OH)_4]^-$ (**R**$_{21}$) than for $Ru^{(III)}(OH)_3$ (**R**$_{15}$). Since the most stable $Ru^{(III)}$ sites in amorphous silica are octahedral with two adsorbed water molecules, water desorption proceeds hydride formation (see **R**$_{14}$ in Fig. 12). The molecular calculations show a significant energy penalty for water desorption of about +45 kJ mol^{-1} (**R**$_{16}$, **R**$_{19}$ and **R**$_{22}$).

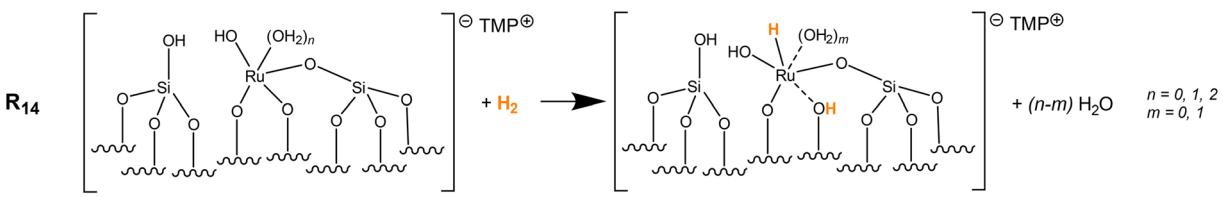

Fig. 12 $Ru^{(III)}$-hydride formation reaction, in the presence of surfactant TMP^+ (**R**$_{14}$). $Ru^{(III)}(O)_3(OH)$ is used as site example.

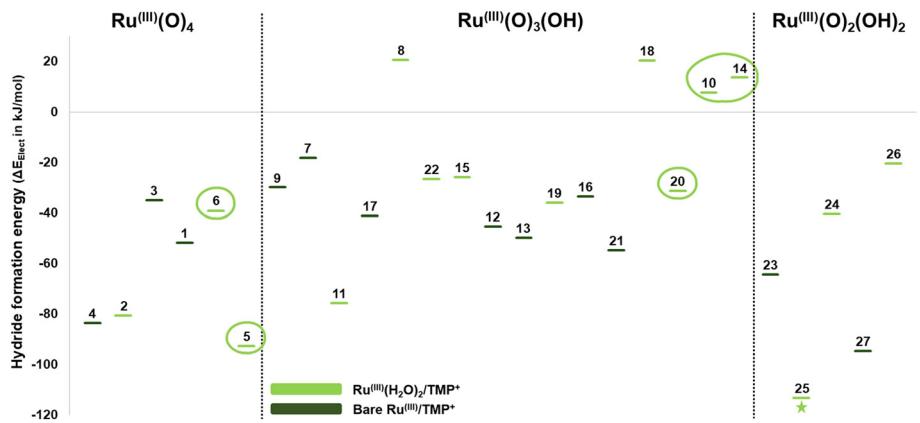

Fig. 13 $Ru^{(III)}$-hydride formation energies for all 27 exchanged $Ru^{(III)}$ sites, in the presence of surfactant TMP^+, according to reaction **R**$_{14}$ in Fig. 12. The star icon indicates sites with only one adsorbed H_2O molecule. Highlighted sites correspond to the most stable $Ru^{(III)}$ sites (Fig. 6). Calculations were performed with PBE-D3(BJ) (VASP) and electronic energies in kJ mol^{-1}.

Table 3 Water desorption and hydride formation reactions using molecular complexes performed with PBE-D3(BJ) and DLPNO-CCSD(T)/Def2-TZVP[a] methods. ΔE_{Elect} values in kJ mol^{-1}

Water desorption and hydride formation reactions		PBE-D3(BJ) (VASP)	DLPNO-CCSD(T)/Def2-TZVP[a]
R_{15}	$Ru(OH)_3 + H_2 \rightarrow Ru(H)(OH)_2(H_2O)$	−28	−45
R_{16}	$Ru(OH)_3(H_2O)_3 \rightarrow Ru(OH)_3(H_2O)_2 + H_2O$	+45	+50
R_{17}	$Ru(OH)_3(H_2O)_2 + H_2 \rightarrow Ru(H)(OH)_2(H_2O)_2 + H_2O$	−47	−1
R_{18}	$[Ru(OH)_4]^-[TMP]^+ + H_2 \rightarrow [Ru(H)(OH)_3(H_2O)]^-[TMP]^+$	−73	−102
R_{19}	$[Ru(OH)_4(H_2O)_2]^-[TMP]^+ \rightarrow [Ru(OH)_4(H_2O)]^-[TMP]^+ + H_2O$	+49	+59
R_{20}	$[Ru(OH)_4(H_2O)]^-[TMP]^+ + H_2 \rightarrow [Ru(H)(OH)_3(H_2O)]^-[TMP]^+ + H_2O$	−44	−50
R_{21}	$[Ru(OH)_4]^- + H_2 \rightarrow [Ru(H)(OH)_3(H_2O)]^-$	−52[b]	−82
R_{22}	$[Ru(OH)_4(H_2O)_2]^- \rightarrow [Ru(OH)_4(H_2O)]^- + H_2O$	+44[b]	+53
R_{23}	$[Ru(OH)_4(H_2O)]^- + H_2 \rightarrow [Ru(H)(OH)_3(H_2O)]^- + H_2O$	−30[b]	−28

Ruthenium is present in its $Ru^{(III)}$ oxidation state in all reactions. [a] Geometry optimizations with PBE-D3(BJ)/Def2-TZVP, followed by single-point calculations using DLPNO-CCSD(T)/Def2-TZVP. [b] PBE-D3(BJ)/Def2-TZVP calculations for charged species using ORCA.

Interestingly, the DLPNO-CCSD(T)/Def2-TZVP desorption energies agree quite well with the PBE-D3(BJ) values. Favorable hydride formation more than compensates this energy cost, leading to an overall reaction energy of −19 to −35 kJ mol^{-1} for the molecular models. This is significantly less favorable than for some of the $Ru^{(III)}$ sites in the periodic slab model (Fig. 13), illustrating the effect of the amorphous silica nature.

Water coordination determines the stability of $Ru^{(III)}$-hydride species by influencing the preferred geometry at each site. Two distinct coordination modes were observed: *trans* and *cis* (Fig. 14). In the *trans* configuration, the partial negative charge on the $Ru^{(III)}$-hydride induces the decoordination of the second H_2O molecule. While additional hydrogen bonding near the site contributes to stability, the removal of this desorbed water molecule results in a significant energy penalty, further destabilizing the hydride species. In contrast, in sites with *cis* configuration, the H_2O molecule remains coordinated to $Ru^{(III)}$.

Within the amorphous silica structure, most $Ru^{(III)}$-hydride structures adopt a square pyramidal (5-coordinated) geometry, which results from the formation of a dative bond or the decoordination of a *trans*-H_2O molecule from the $Ru^{(III)}$ center. The desorption of a *trans*-H_2O results in an energy cost for many $Ru^{(III)}$-hydrides, for example at sites 6, 8, 10 and 14 (Fig. 13).

The stability of $Ru^{(III)}$-hydrides in $Ru^{(III)}(O)_4$ groups is strongly influenced by the size of the surrounding silica rings. Hydride species at sites 2 and 4 show high stability due to the opening of one of the 4-Si rings, which relieves structural strain by dative bond formation. Despite similar formation energies, their geometries differ: site 2 adopts a square pyramidal structure, while site 4 forms a 4-coordinated, T-shape geometry (Fig. 15).

Ring size also affects the stability of a few $Ru^{(III)}$-hydride species within $Ru^{(III)}(O)_3(OH)$ and $Ru^{(III)}(O)_2(OH)_2$ groups. At sites 11 and 16, opening of 4-membered silica rings stabilizes the structure through dative bond formation. At site 25, the formation of the hydride is highly favored due to the strain relief from the opening of a 9-membered silica ring, which results in an optimal square pyramidal geometry.

For other $Ru^{(III)}$ structures, the proton from hydrogen activation goes to a hydroxyl group, forming an H_2O molecule. At site 9, the water molecule stabilizes the hydride structure, while at site 23, H_2O formation is the only stable configuration (dative bond formation is unfavorable).

Sites 5, 6, 10, 14 and 20 have been identified as the most likely $Ru^{(III)}$ sites in amorphous silica (Fig. 6). For sites 10 and 14, the desorption of water brings a significant energy cost, making it difficult to release a H_2O molecules and make space for the hydride. As a result, $Ru^{(III)}$ at sites 10 and 14 are stable but not active. In contrast, hydride formation at sites

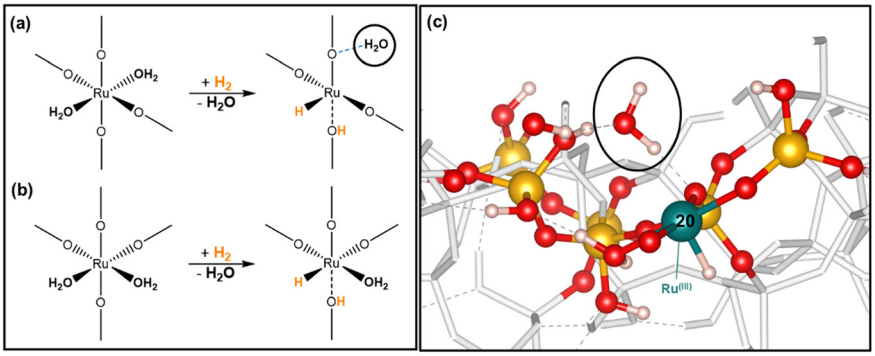

Fig. 14 Coordination of two H_2O molecules in a 6-coordinated $Ru^{(III)}$ complex: (a) *trans*, and (b) *cis* configuration; (c) $Ru^{(III)}$-hydride at site 20, in the presence of surfactant. Example for the *trans* configuration in (a), where the H_2O molecule desorbs from $Ru^{(III)}$ but stays nearby. TMP^+ molecule not shown in the figure.

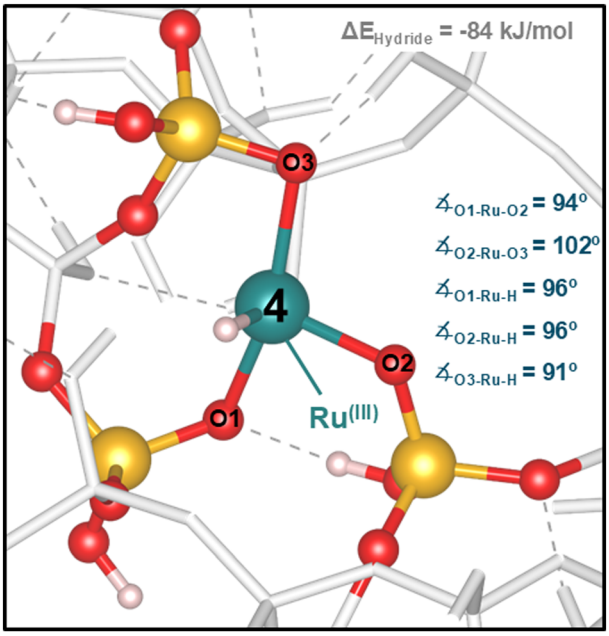

Fig. 15 Ru$^{(III)}$-hydride at site 4 (no adsorbed H_2O molecules), in the presence of surfactant. O–Ru–H bond angles indicated in the figure. TMP^+ not shown in the figure.

5, 6 and 20 is energetically favorable, suggesting that these Ru$^{(III)}$ sites are both synthesizable and active. This lack of an expected correlation between site stability and hydride affinity is illustrated by plotting site stability (Si-to-Ru$^{(III)}$ exchange energy) against hydride formation energy (Fig. S11†), which highlights the broad range of Ru$^{(III)}$ site stabilities and hydride affinities. It also shows that site stability alone does not guarantee catalytic activity. Some of the most stable sites lead to very unstable hydride species, suggesting that these sites are likely formed but remain inactive, while others demonstrate a strong affinity for hydride formation.

3.4.1. Hydride formation at grafted Ru$^{(III)}$ sites. The formation of Ru$^{(III)}$-hydride species on grafted Ru$^{(III)}$ sites was analyzed for the most stable Ru$^{(III)}(O)_2(OH)_2$, Ru$^{(III)}(O)_3(OH)$, and Ru$^{(III)}(O)_4$ structures (Fig. 16). The results suggest that the formation of hydrides on grafted Ru$^{(III)}$ sites is less favorable than the formation on exchanged Ru$^{(III)}$ sites. Among the grafted structures, Ru$^{(III)}(O)_4$ is the least stable initially; however hydride formation is quite favorable on this site, releasing some of the strain in the structure by breaking a Si–O–Ru bond to form Si–OH (Fig. 16).

The most stable grafted Ru$^{(III)}(O)_3(OH)$ structure is the only octahedral grafted site. Water decoordination hinders hydride formation at this site. On the most stable grafted Ru$^{(III)}(O)_2(OH)_2$ site, hydride formation appears to be favorable.

The nature of the amorphous silica dictates the stability of the Ru$^{(III)}$ sites; however, predicting which of these sites will also be active in hydrogenation reactions remains challenging as there is no correlation between site stability and affinity for hydride formation. Indeed, sites 5, 6 and 20 show both favorable exchange energies and favorable hydride formation, while sites 10 and 14 are preferred Ru$^{(III)}$ locations, but show limited affinity for hydride formation. As a result, calculations are essential to pinpoint the specific site characteristics that enable both stability and activity of Ru$^{(III)}$ sites incorporated in amorphous silica.

4. Conclusions

The solid micellar Ru$^{(III)}$@MCM-41 catalyst consists of isolated Ru$^{(III)}$ single-sites and silanoxo basic sites incorporated into the walls of amorphous MCM-41, and stabilized by quaternary ammonium surfactant molecules (CTA^+) inside the pores.

The complex structure of amorphous silica makes it challenging to identify and characterize the active sites in this catalyst material. Thus, computational models that capture the heterogeneity of sites in amorphous silica-supported catalysts are essential to understand the factors that determine stability and activity in this class of materials.

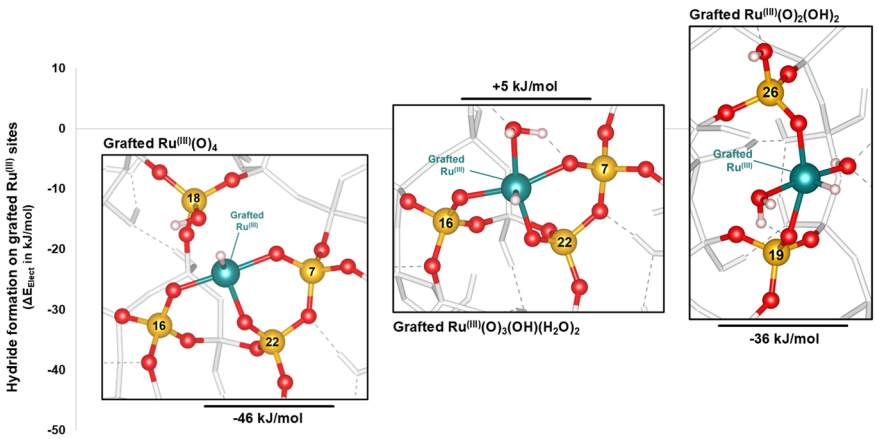

Fig. 16 Ru$^{(III)}$-hydride formation energies for the most stable grafted Ru$^{(III)}(O)_4$, Ru$^{(III)}(O)_3(OH)(H_2O)_2$ and Ru$^{(III)}(O)_2(OH)_2$ sites, in the presence of surfactant TMP^+, according to reaction $\mathbf{R_{14}}$ in Fig. 12. Calculations were performed with PBE-D3(BJ) (VASP) and electronic energies in kJ mol^{-1}. TMP^+ not shown in the figure.

The amorphous hydroxylated silica model used in this work begins to describe the complexity of $Ru^{(III)}$@MCM-41. Amorphous silica features a wide heterogeneity of sites that $Ru^{(III)}$ can occupy. Periodic slab models account for geometric factors (*e.g.*, ring strain) and long-range effects, such as interactions between neighboring silanol groups and hydrogen bonding. This allows for a comprehensive understanding of how ring strain, hydrogen bonding, and coordination environment influence the stability and activity of $Ru^{(III)}$ single-sites in amorphous silica. The size of the silica rings is particularly important. Exchanging the tetrahedral Si with an octahedral $Ru^{(III)}$ site causes structural deformation due to strain in the Si rings. Ring strain appears to play a significant role in the relative stability of $Ru^{(III)}(O)_4$ sites, but is less pronounced for $Ru^{(III)}(O)_3(OH)$ and $Ru^{(III)}(O)_2(OH)_2$ sites, where hydrogen bonding becomes particularly significant, especially in $Ru^{(III)}(O)_2(OH)_2$.

The effect of the surfactant was evaluated by replacing the TMP^+ counterion with H^+, simulating a surfactant-free environment. While the factors governing site stability remain similar to those observed with the surfactant, Si-to-$Ru^{(III)}$ exchange energies were overall less favorable with H^+ as the counterion, highlighting the stabilizing role of TMP^+. Molecular complex calculations also showed that while condensation of $Ru^{(III)}(OH)_3(H_2O)_3$ with $Si(OH)_4$ is favorable, condensation is significantly more favorable with $[Ru^{(III)}(OH)_4]^-[TMP]^+$.

Using a periodic amorphous hydroxylated silica model, we identify that single-site $Ru^{(III)}$ in MCM-41 preferably adopts an octahedral geometry, with the adsorption of two H_2O molecules, either as $Ru^{(III)}(O)_4(H_2O)_2$ or $Ru^{(III)}(O)_3(OH)(H_2O)_2$. Such sites are located within larger silica rings, which facilitates octahedral coordination geometry without constraints, and near hydroxylated regions of the amorphous structure, enabling hydrogen bonding interactions. These findings align with the favorable condensation of $Ru^{(III)}$ with $Si(OH)_4$ in the presence of surfactant, which promotes the formation of multiple Si–O–Ru bonds.

The presence of two $Ru^{(III)}$ per unit cell was also analyzed, confirming that their relative positioning does not prevent each $Ru^{(III)}$ site from adopting a square planar geometry, even when they are adjacent to each other.

For grafted $Ru^{(III)}$ sites, the optimal distance between silanol groups, particularly those outside highly hydroxylated areas, allows the formation of grafted $[Ru^{(III)}(O)_2(OH)_2]^-[TMP]^+$ and $[Ru^{(III)}(O)_3(OH)]^-[TMP]^+$ sites. Nevertheless, when comparing the energies of Si-to-$Ru^{(III)}$ exchange and grafting of $Ru^{(III)}$, the exchanged sites remain among the most stable sites of all calculated configurations.

The hydroxylated amorphous silica model captures a diverse range of exchanged and grafted $Ru^{(III)}$ sites, providing insights into the factors that govern their stability and activity. We find that no single structural descriptor fully captures the stability of $Ru^{(III)}$ sites within the amorphous silica walls.

The local environment plays a decisive role, as the stability of these sites arises from a balance between the condensation favoring multiple Si–O–Ru bonds and the opposing effects of ring strain and hydrogen bonding that hinder full condensation.

This work highlights the importance of square planar and octahedral geometries in facilitating the favorable exchange or grafting of $Ru^{(III)}$ on amorphous silica. When the local environment fails to accommodate these geometries, ring strain or steric repulsion can limit $Ru^{(III)}$ coordination preferences.

However, site stability alone does not guarantee catalytic activity. Interestingly, some of the stable exchanged $Ru^{(III)}(O)_4(H_2O)_2$ and $Ru^{(III)}(O)_3(OH)(H_2O)_2$ sites also demonstrate a strong affinity for hydrogen activation, leading to favorable hydride formation. Dual consideration of stability and activity is important when modeling catalysts.

The amorphous silica model provides a framework for exploring the distribution of possible single $Ru^{(III)}$ sites likely present in $Ru^{(III)}$@MCM-41 and also captures the stabilizing role of the surfactant in this class of materials.

Data availability

Additional figures, tables, energy diagrams and analysis are described in the ESI† document. Coordinates of the structures are available upon request.

Conflicts of interest

There are no conflicts to declare.

Acknowledgements

S. S. is grateful to the Flemish Research Foundation (FWO) for financial support for the doctoral fellowship grant (1SA4124N). The computational resources and services used in this work were provided by the VSC (Flemish Supercomputer Center), funded by the Research Foundation Flanders (FWO), and the Flemish Government – department EWI. V. V. O. acknowledges the financial support of the French National Research Agency (DEZECO, Ref. ANR-22-CE05-0005). F. T. also wishes to acknowledge the Vrije Universiteit Brussel for support, among other, through a Strategic Research Program awarded to his group.

References

1 F. Tielens, in *Chemistry of Silica and Zeolite-Based Materials*, ed. A. Douhal and M. Anpo, Elsevier, 2019, vol. 2, pp. 351–374.
2 B. R. Goldsmith, B. Peters, J. K. Johnson, B. C. Gates and S. L. Scott, *ACS Catal.*, 2017, **7**, 7543–7557.
3 F. Tielens, M. Gierada, J. Handzlik and M. Calatayud, *Catal. Today*, 2020, **354**, 3–18.
4 C. Vandervelden, A. Jystad, B. Peters and M. Caricato, *Ind. Eng. Chem. Res.*, 2021, **60**, 12834–12846.

5 S. A. Khan, S. M. Godahewa, P. N. Wimalasiri, W. H. Thompson, S. L. Scott and B. Peters, *Chem. Mater.*, 2022, **34**, 3920–3930.
6 S. Srinivas, K. Srivastava, K. Yu, D. G. Vlachos and S. Caratzoulas, *ACS Catal.*, 2023, **13**, 15641–15651.
7 B. E. Leonhardt, M. Head-Gordon and A. T. Bell, *ACS Catal.*, 2024, **14**, 3049–3064.
8 U. Das, G. Zhang, B. Hu, A. S. Hock, P. C. Redfern, J. T. Miller and L. A. Curtiss, *ACS Catal.*, 2015, **5**, 7177–7185.
9 F. Tielens, C. Gervais, J. F. Lambert, F. Mauri and D. Costa, *Chem. Mater.*, 2008, **20**, 3336–3344.
10 M. Gierada, I. Petit, J. Handzlik and F. Tielens, *Phys. Chem. Chem. Phys.*, 2016, **18**, 32962–32972.
11 L. T. Zhuravlev, *Colloids Surf., A*, 2000, **173**, 1–38.
12 P. Ugliengo, M. Sodupe, F. Musso, I. J. Bush, R. Orlando and R. Dovesi, *Adv. Mater.*, 2008, **20**, 4579–4583.
13 C. S. Ewing, S. Bhavsar, G. Veser, J. J. McCarthy and J. K. Johnson, *Langmuir*, 2014, **30**, 5133–5141.
14 A. Comas-Vives, *Phys. Chem. Chem. Phys.*, 2016, **18**, 7475–7482.
15 M. M. Islam, D. Costa, M. Calatayud and F. Tielens, *J. Phys. Chem. C*, 2009, **113**, 10740–10746.
16 A. Wojtaszek, I. Sobczak, M. Ziolek and F. Tielens, *J. Phys. Chem. C*, 2010, **114**, 9002–9007.
17 H. Guesmi and F. Tielens, *J. Phys. Chem. C*, 2012, **116**, 994–1001.
18 C. S. Ewing, A. Bagusetty, E. G. Patriarca, D. S. Lambrecht, G. Veser and J. K. Johnson, *Ind. Eng. Chem. Res.*, 2016, **55**, 12350–12357.
19 L. Floryan, A. P. Borosy, F. Núñez-Zarur, A. Comas-Vives and C. Copéret, *J. Catal.*, 2017, **346**, 50–56.
20 T. Siodla, I. Sobczak, M. Ziolek and F. Tielens, *Microporous Mesoporous Mater.*, 2018, **256**, 199–205.
21 K. Kurleto, F. Tielens and J. Handzlik, *J. Phys. Chem. C*, 2020, **124**, 3002–3013.
22 C. S. Praveen, A. P. Borosy, C. Copéret and A. Comas-Vives, *Inorg. Chem.*, 2021, **60**, 6865–6874.
23 F. S. Brigiano, M. Gierada, F. Tielens and F. Pietrucci, *ACS Catal.*, 2022, **12**, 2821–2830.
24 X. Deraet, J. Turek, M. Alonso, F. Tielens, S. Cottenier, P. W. Ayers, B. M. Weckhuysen and F. De Proft, *Chem. – Eur. J.*, 2021, **27**, 6050–6063.
25 Q. Wang, S. Santos, C. A. Urbina-Blanco, W. Y. Hernández, M. Impéror-Clerc, E. I. Vovk, M. Marinova, O. Ersen, W. Baaziz, O. V. Safonova, A. Y. Khodakov, M. Saeys and V. V. Ordomsky, *Appl. Catal., B*, 2021, **290**, 120036.
26 Q. Wang, S. Santos, C. A. Urbina-Blanco, W. Zhou, Y. Yang, M. Marinova, S. Heyte, T.-R. Joelle, O. Ersen, W. Baaziz, O. V. Safonova, M. Saeys and V. V. Ordomsky, *Appl. Catal., B*, 2022, **300**, 120730.
27 Q. Wang, C. M. De Brito Mendes, O. V. Safonova, W. Baaziz, C. A. Urbina-Blanco, D. Wu, M. Marinova, O. Ersen, M. Capron, A. Y. Khodakov, M. Saeys and V. V. Ordomsky, *J. Catal.*, 2023, **426**, 336–344.
28 G. Kresse and J. Furthmüller, *Phys. Rev. B: Condens. Matter Mater. Phys.*, 1996, **54**, 11169–11186.
29 M. Ernzerhof and G. E. Scuseria, *J. Chem. Phys.*, 1999, **110**, 5029–5036.
30 S. Grimme, S. Ehrlich and L. Goerigk, *J. Comput. Chem.*, 2011, **32**, 1456–1465.
31 G. Kresse and D. Joubert, *Phys. Rev. B: Condens. Matter Mater. Phys.*, 1999, **59**, 1758–1775.
32 F. Neese, *Wiley Interdiscip. Rev.: Comput. Mol. Sci.*, 2022, **12**, e1606.
33 F. Weigend and R. Ahlrichs, *Phys. Chem. Chem. Phys.*, 2005, **7**, 3297–3305.
34 C. Riplinger, P. Pinski, U. Becker, E. F. Valeev and F. Neese, *J. Chem. Phys.*, 2016, **144**, 024109.
35 R. H. Crabtree, *The Organometallic Chemistry of the Transition Metals*, Wiley, New York, 2014, pp. 40–68.
36 D. R. Aireddy and K. Ding, *ACS Catal.*, 2022, **12**, 4707–4723.